



HAL
open science

Discontinuous Galerkin finite element method applied to the coupled unsteady Stokes/Cahn-Hilliard equations

Franck Pigeonneau, Elie Hachem, Pierre Saramito

► To cite this version:

Franck Pigeonneau, Elie Hachem, Pierre Saramito. Discontinuous Galerkin finite element method applied to the coupled unsteady Stokes/Cahn-Hilliard equations. 2018. hal-01773404v1

HAL Id: hal-01773404

<https://hal.science/hal-01773404v1>

Preprint submitted on 21 Apr 2018 (v1), last revised 14 Feb 2019 (v2)

HAL is a multi-disciplinary open access archive for the deposit and dissemination of scientific research documents, whether they are published or not. The documents may come from teaching and research institutions in France or abroad, or from public or private research centers.

L'archive ouverte pluridisciplinaire **HAL**, est destinée au dépôt et à la diffusion de documents scientifiques de niveau recherche, publiés ou non, émanant des établissements d'enseignement et de recherche français ou étrangers, des laboratoires publics ou privés.

Discontinuous Galerkin finite element method applied to the coupled unsteady Stokes/Cahn-Hilliard equations

F. Pigeonneau^{a,*}, E. Hachem^a, P. Saramito^b

^a*MINES ParisTech, PSL Research University, CEMEF - Centre de mise en forme des matériaux, CNRS UMR 7635, CS 10207, Claude Daunesse 06904 Sophia Antipolis cedex, France*

^b*CNRS and Lab. J. Kuntzmann, B.P. 53, 38041 Grenoble cedex 9, France*

Abstract

Two-phase flows driven by the interfacial dynamics are studied with a phase-field model to implicitly track interfaces in the framework of the Cahn-Hilliard theory. The fluid dynamics is described by the Stokes equations with an additional source term in the momentum equation taking into account the capillary forces. A discontinuous Galerkin finite element method is used to solve the coupled Stokes/Cahn-Hilliard equations. The Cahn-Hilliard equation is treated as a system of two coupled equations corresponding to the advection-diffusion equation for the phase field and a non-linear elliptic equation for the chemical potential. First, the variational formulation of the Cahn-Hilliard equation is presented. A numerical test is achieved showing the optimal-order in error bounds. Second, the variational formulation in discontinuous Galerkin finite element approach of the Stokes equations is recalled in which the same space of approximation is used for the velocity and the pressure with an adequate stabilization technique. The rates of convergence in space and time are evaluated leading to an optimal-order in error bounds in space and a second order in time with a backward differential formula at the second order. Numerical tests devoted to two-phase flows are provided on ellipsoidal droplet retraction and on the capillary rising in a tube.

Keywords: two-phase flow, phase-field theory, finite element, discontinuous Galerkin, droplet retraction, capillary rising

*Corresponding author: Tel. +33 (4) 93 95 74 34, Fax +33 (4) 92 38 97 52.

Email addresses: franck.pigeonneau@mines-paristech.fr (F. Pigeonneau),
elie.hachem@mines-paristech.fr (E. Hachem), Pierre.Saramito@imag.fr (P. Saramito)

Preprint submitted to J. Comput. Phys.

April 21, 2018

1. Introduction

Two-phase flows occur in many industrial processes as in metallurgy, nuclear plants, polymer and glass processing but also in nature such as volcano eruptions, ocean dynamics. An accurate description of interfaces between immiscible fluids becomes more and more important to study the wetting or dewetting on a substrate which can be chemically heterogeneous or structured at microscale or nanoscale. To guide the designer, numerical solvers of industrial processes need to be more and more accurate based on a complex physics coupling various phenomena.

The dynamics of two-phase flows driven by the capillary forces can be addressed by various numerical methods which can be sorted as a function of the method to track interfaces [16]. A first class of methods tracks explicitly interfaces using boundary integral method in the limit of vanishing Reynolds number [29, 28] or front tracking method [39] when the Reynolds number is finite. This approach is based on the Lagrangian description of interfaces. Despite of the high level of accuracy of these techniques, the topological changes are difficult to take into account. Moreover, the dynamics of contact line stays difficult. A second class of methods tracks interfaces implicitly with a volume marker like the “Volume of Fluid” technique initially developed by Hirt and Nichols [19] or by a “level-set” method [33, 34]. They are based on the Eulerian description and can straightforward describe topological changes like coalescence or break-up of bubbles or drops. More recently, the behavior of the triple line has been implemented with success in Volume of Fluid approach [25] or with level-set technique in [36].

In the two previous approaches, interfaces are considered as sharp-interfaces without volume leading to a singular behavior at the triple line, Huh-Scriven’s paradox [21]. To regularize the physics at the triple line, a slip length is commonly introduced [9]. To overcome this kind of singularity, an alternative method considers interface with a small thickness. This technique employs the concept of “phase-field” introduced initially in statistical physics to describe phase change or spinodal decomposition [7]. The development of the phase-field method in fluid mechanics has been summarized by Anderson et al. [2]. One of the first contribution of the application of the phase-field theory to two-phase flows has been done by Antanovskii [3]. One of the main advantages of the phase-field method is that the normal and the curvature are not needed to determine the

capillary forces involved in the momentum equation.

This technique is also particularly well-adapted to study interaction with a solid substrate. The contact-line dynamics has been studied by Sepecher [32] who showed that the removal of the singularity at the triple line is due to a mass transfer across the interface combined with a finite thickness of the interface. Jacqmin [23] studied the dynamics of contact-line using the diffuse interface investigating the behaviors of the phase-field and the chemical potential close to the triple line. A variational formulation has been proposed by Qian et al. [30] mainly to generalize the boundary condition on the velocity. Yue et al. [43] and Yue and Feng [42] studied the effect of the diffuse thickness to represent adequately the sharp-interface limit.

The numerical resolution of the Cahn-Hilliard coupled to Navier-Stokes equations in the case of complex geometries is not so simple because the Cahn-Hilliard equation is a non-linear and biharmonic equation. Since the typical size over which the phase field changes across the interface is small, the numerical space resolution has to be important. Moreover, far away interface, the diffusion of the chemical potential is weak meaning that the Cahn-Hilliard equation is a quasi-pure transport equation. Jacqmin [22] implemented a compact-finite difference scheme to solve the Cahn-Hilliard/Navier-Stokes equations. Badalassi et al. [4] developed a time-splitting method with a spectral method in space.

For the present work, a discontinuous Galerkin finite element method has been used. The main feature of the technique is to have an accurate mass conservation applied to convective equation [38]. The numerical computation using a discontinuous Galerkin method to solve the phase-field model has been initiated by Feng and Karakashian [13] among others. They established an optimal-order error bound by solving the fourth-order equation when the polynomial degree is greater or equal to two. Kay et al. [24] solved the Cahn-Hilliard equation as a system of two second-order equations. This method is close to the technique to solve biharmonic equations splitting in two elliptic equations. Gudi et al. [17] employ this method with a discontinuous Galerkin method and they prove the existence and uniqueness of the discrete problem.

In this present work, and since the phase-field method is devoted to study the fluid dynamics at small scale, the fluid inertia can be neglected. Consequently, we investigate the numerical method to solve the coupled Stokes/Cahn-Hilliard equations with a discon-

tinuous Galerkin finite element technique. Due to the viscosity variation over interfaces, the generalization of the Stokes formulation is provided for heterogeneous viscosity. We focus our investigation on the accuracy of the numerical solver and on the interaction between the two phases and a substrate. A particular attention will be also devoted to the mass conservation.

We start by the problem statement in section 2 in which the Stokes/Cahn-Hilliard equations will be recalled. The numerical method to solve only the phase-field will be presented in section 3 with a test to determine the numerical errors. Section 4 is devoted to the numerical method of the coupled Stokes/Cahn-Hilliard equations. The space and time rates of convergence will be also studied. Two-phase flows will be investigated in section 5 with a first example describing the droplet retraction and a second case devoted to a capillary rising in which the flow is driven by the contact line dynamics.

2. Two-phase flows modeling with a phase-field formulation

Two phases are considered with respectively a density ρ_1 and a dynamic viscosity η_1 for the phase 1 and ρ_2 and η_2 for the phase 2. The phase field method considers that the shift between the two phases occurs over a thin layer equal to ζ corresponding to the “diffuse interface” thickness. Conventionally, the phase 1 is taken as the heavy phase, i.e. $\rho_1 > \rho_2$. In a space domain, $\Omega \subset \mathbb{R}^d$ with a boundary $\partial\Omega$ and $d = 2$ or 3 , the phase at any material point with a position \mathbf{x} and at each time t is described by an “order parameter” $\varphi(\mathbf{x}, t)$. By convention, the phase 1 is given by the order parameter $\varphi = 1$ and the phase 2 by $\varphi = -1$. The function φ can be seen also as a volume fraction meaning that the density written at every point of Ω is given by

$$\rho(\varphi) = \frac{\rho_1 + \rho_2}{2} + \frac{\rho_1 - \rho_2}{2}\varphi. \quad (1)$$

The dynamic viscosity is generally given as a function of φ as follows

$$\eta(\varphi) = \frac{\eta_1 + \eta_2}{2} + \frac{(\eta_1 - \eta_2)}{2}\varphi. \quad (2)$$

Under the actions of external forces, boundary conditions and interaction between the two phases, the media changes in space and time requiring the balance equations of mass

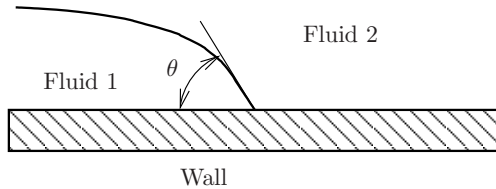


Figure 1: Sketch of the triple line between phases 1 and 2 and the wall. The contact angle is written θ .

and momentum. Moreover, the dynamics between the two phases has to be considered by writing an equation on the phase field φ .

Let start by the description from the thermodynamic equilibrium point of view. The total free energy of the system writes as a functional of φ and its gradient as follows [23, 43]

$$\mathcal{F}[\varphi] = \int_{\Omega} f_m(\varphi, \nabla\varphi) dV + \int_{\partial\Omega_w} f_w(\varphi) dS, \quad (3)$$

Functions $f_m(\varphi, \nabla\varphi)$ and $f_w(\varphi)$ are respectively the mixing free energy in volume and the wall free energy [6, 23]. The boundary $\partial\Omega_w$ is a part of $\partial\Omega$ corresponding to walls.

The volume energy takes into account energies of each phase with stable states found for $\varphi = \pm 1$ and the contribution due to interfaces. According to the pioneer work of van der Waals [40], $f_m(\varphi, \nabla\varphi)$ is written as

$$f_m(\varphi, \nabla\varphi) = \frac{\lambda}{4\zeta^2} (\varphi^2 - 1)^2 + \frac{\lambda}{2} \|\nabla\varphi\|^2, \quad (4)$$

for which λ is an energy by unit of length. Remark that the first term of the right-hand side of (4) is double-well potential with two local minimum in $\varphi = \pm 1$. The wall energy $f_w(\varphi)$ takes into account a triple line when the two phases are in contact with a wall. In this case, the geometry of the interface has to verify a physical requirement as shown in Figure 1. According to the Young-Dupré, the equilibrium contact angle θ is given by [10]

$$\cos \theta = \frac{\sigma_{w2} - \sigma_{w1}}{\sigma}, \quad (5)$$

for which σ is the surface tension between the two phases, σ_{w1} the surface energy between the phase 1 and the wall and σ_{w2} the surface energy between the phase 2 and the wall.

The wall energy describing the wetting physics at the equilibrium is given by the

relation [6]

$$f_w(\varphi) = -\sigma \cos \theta \frac{\varphi(3 - \varphi^2)}{4} + \frac{\sigma_{w1} + \sigma_{w2}}{2}, \quad (6)$$

The equilibrium state is obtained when the functional \mathcal{F} is a minimum. The variational derivative (see [15]) of \mathcal{F} allows to define two relations

$$\mu(\varphi) = \lambda \left[\frac{\varphi(\varphi^2 - 1)}{\zeta^2} - \nabla^2 \varphi \right], \quad \forall \mathbf{x} \in \Omega, \quad (7)$$

$$L(\varphi) = \lambda \nabla \varphi \cdot \mathbf{n} - \frac{3(1 - \varphi^2)\sigma}{4} \cos \theta, \quad \forall \mathbf{x} \in \partial\Omega_w, \quad (8)$$

for which equation (7) defines the chemical potential in the bulk and equation (8) the wall chemical potential [30]. In the equilibrium state, both (7) and (8) have to be equal to zero.

In one dimension case where the interface is defined on $x = 0$, the equilibrium phase field is obviously given by the following solution

$$\varphi(x) = \tanh \left(\frac{x}{\sqrt{2}\zeta} \right). \quad (9)$$

The macroscopic surface tension between the two fluids already introduced above is defined by

$$\sigma = \lambda \int_{-\infty}^{\infty} \left(\frac{d\varphi}{dx} \right)^2 dx, \quad (10)$$

which gives with the solution (9) [43]

$$\sigma = \frac{2\sqrt{2}}{3} \frac{\lambda}{\zeta}. \quad (11)$$

This last equation is very important since it links a macroscopic property σ and microscopic quantities λ and ζ .

For vanishing inertia, the fluid dynamics has to be described thanks to the Stokes equations in which the source term due to interfaces must be introduced. The generalization of the Cahn-Hilliard equations coupled to the Navier-Stokes equations is described by the ‘‘model H’’ according to the nomenclature of Hohenberg and Halperin [20]. In the

case of incompressible fluids, the model takes the following form

$$\nabla \cdot \mathbf{u} = 0, \quad (12)$$

$$-\nabla P + \nabla \cdot [2\eta(\varphi)\mathbf{D}(\mathbf{u})] + \rho(\varphi)\mathbf{g} + \mu\nabla\varphi = 0, \quad (13)$$

$$\frac{\partial\varphi}{\partial t} + \nabla\varphi \cdot \mathbf{u} = \nabla \cdot [M(\varphi)\nabla\mu(\varphi)], \quad (14)$$

$$\mu(\varphi) = \frac{\lambda}{\zeta^2} [\varphi(\varphi^2 - 1) - \zeta^2\nabla^2\varphi]. \quad (15)$$

where \mathbf{u} is the velocity field, P the pressure taking into account the part of the chemical potential deriving from a potential. Equation (12) describes the mass conservation for which each fluid is assumed incompressible. Equation (13) corresponds to the momentum balance. The second term of the right-hand side of (13) is the viscous stress for which $\mathbf{D}(\mathbf{u})$ is the rate-of-strain tensor given by

$$\mathbf{D} = \frac{1}{2} (\nabla\mathbf{u} + {}^t\nabla\mathbf{u}). \quad (16)$$

The third term of (13) is the volume force due to gravity in which \mathbf{g} is the gravitational acceleration and the last term of (13) is the capillary force related to the chemical potential and the gradient of the order parameter. A demonstration of the momentum equation in the framework of phase field formulation can be found in [18].

Equation (14) is the Cahn-Hilliard equation which has to be coupled to the last equation (15) corresponding to the chemical potential. The quantity $M(\varphi)$ is the Onsager mobility.

Equations (12-15) have to be completed by initial and boundary conditions. For the velocity, the no-slip conditions will be used in the following. For the chemical potential, the variational formulation of the Cahn-Hilliard equation gives the natural boundary condition

$$\frac{\partial\mu}{\partial n} = 0, \quad \forall \mathbf{x} \in \partial\Omega, \quad (17)$$

meaning that flux of the chemical potential is equal to zero on the boundary.

For the order parameter, if we assume that on the wall the equilibrium is reached at

any time, the boundary condition writes

$$\lambda \nabla \varphi \cdot \mathbf{n} = \frac{3(1 - \varphi^2)\sigma}{4} \cos \theta, \quad \forall \mathbf{x} \in \partial\Omega_w, \quad (18)$$

which gives that at the interface between the two fluids given by $\varphi = 0$, the dot product of the normal at the interface with the outward normal at the wall is proportional to the cosinus of θ . Outside of interface, the boundary condition is reduced to an homogeneous Neumann condition.

In the following, the Stokes/Cahn-Hilliard equations are written under dimensionless form with a characteristic length L , velocity U , viscosity η_1 and density ρ_1 which will be provided in the numerical examples presented in section 5. The Onsager mobility is assumed constant. The chemical potential is reduced by using the ratio λ/ζ^2 . The time is normalized by L/U . The coupled system of equations is given by in which dimensionless variables are written with the same notation as previously

$$\begin{aligned} \nabla \cdot \mathbf{u} &= 0, & (19) \\ -\nabla P + \nabla \cdot [2\eta(\varphi)\mathbf{D}(\mathbf{u})] + \frac{\text{Bo}}{\text{Ca}} \rho(\varphi)\mathbf{g} + \frac{3}{2\sqrt{2}\text{Ca}\text{Cn}} \mu \nabla \varphi &= 0, \\ \frac{\partial \varphi}{\partial t} + \nabla \varphi \cdot \mathbf{u} &= \frac{1}{\text{Pe}} \nabla^2 \mu(\varphi), & (20) \\ \mu(\varphi) &= \varphi(\varphi^2 - 1) - \text{Cn}^2 \nabla^2 \varphi. & (21) \end{aligned}$$

Six dimensionless numbers arise defined by

$$\text{Bo} = \frac{\rho_1 g L^2}{\sigma}, \quad (22) \quad \text{Ca} = \frac{\eta_1 U}{\sigma}, \quad (23) \quad \text{Pe} = \frac{U \zeta^2 L}{M \lambda}, \quad (24)$$

$$\text{Cn} = \frac{\zeta}{L}, \quad (25) \quad \hat{\rho} = \frac{\rho_2}{\rho_1}, \quad (26) \quad \hat{\eta} = \frac{\eta_2}{\eta_1}. \quad (27)$$

The Bond number Bo measures the ratio of gravity to surface tension forces characterized by the surface tension σ while the capillary number Ca compares the viscosity effect to the surface tension one. The fourth dimensionless number Pe is a Péclet number comparing the diffusion time scale of the chemical potential to the convective time scale which is always greater than one. The Cahn number Cn is the ratio of the

diffuse-interface thickness ζ to the characteristic length scale. The normalized density and dynamic viscosity are given by an arithmetic average:

$$\rho(\varphi) = \frac{1 + \hat{\rho}}{2} + \frac{1 - \hat{\rho}}{2} \varphi, \quad (28)$$

$$\eta(\varphi) = \frac{1 + \hat{\eta}}{2} + \frac{1 - \hat{\eta}}{2} \varphi. \quad (29)$$

3. Numerical resolution of Cahn-Hilliard equation

The numerical method is first focused on the Cahn-Hilliard equation which is a non-linear fourth-order partial differential equation needing a high level of regularity. Since the diffusion of the chemical potential is very weak outside interfaces, the parabolic behavior due to the advection term is important. Consequently, a discontinuous Galerkin finite element method has been chosen to solve the Cahn-Hilliard equation. In this section, we consider the Cahn-Hilliard equation advected with a known solenoidal velocity field \mathbf{u} .

3.1. Discontinuous Galerkin finite element formulation

The continuous problem is

Problem 1 (Cahn-Hilliard problem). Find $\varphi(\mathbf{x}, t)$ and $\mu(\mathbf{x}, t)$ defined in $\Omega \times [0, T]$ such as

$$\frac{\partial \varphi}{\partial t} + \mathbf{u} \cdot \nabla \varphi - \frac{1}{\text{Pe}} \nabla^2 \mu(\varphi) = 0, \text{ in } \Omega \times [0, T], \quad (30)$$

$$-\mu(\varphi) + \varphi(\varphi^2 - 1) - \text{Cn}^2 \nabla^2 \varphi = 0, \text{ in } \Omega \times [0, T], \quad (31)$$

$$\varphi(\mathbf{x}, t = 0) = \varphi_0(\mathbf{x}), \text{ in } \Omega, \quad (32)$$

$$\frac{\partial \varphi}{\partial n} = f(\varphi), \text{ on } \partial\Omega, \quad (33)$$

$$\frac{\partial \mu}{\partial n} = 0, \text{ on } \partial\Omega. \quad (34)$$

Moreover, the normal component of the velocity $\mathbf{u} \cdot \mathbf{n}$ is equal to zero on $\partial\Omega$ for \mathbf{n} the outward unit normal on $\partial\Omega$. The boundary condition on φ , eq. (33), has been taken in general form because in applications the interaction with a wall for instance involves a condition on normal derivative as presented above.

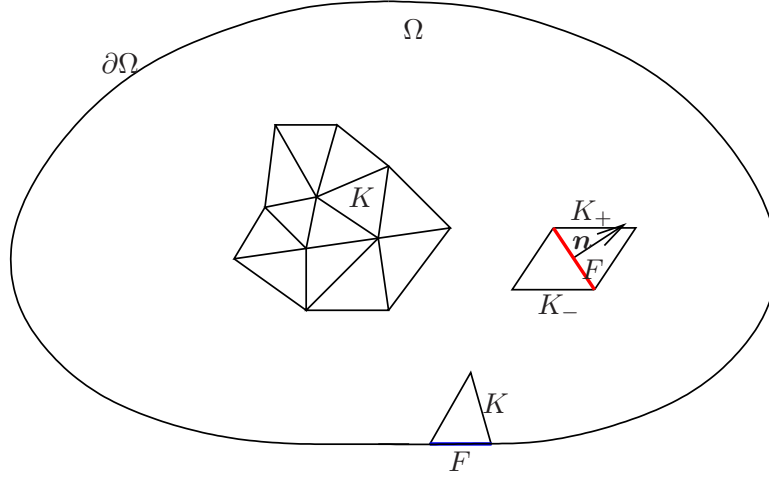


Figure 2: Triangulation of the domain Ω and representation of interior faces in red and boundary faces in blue. The orientation of the interior normal between two triangles K_+ and K_- is also drawn.

A discontinuous Galerkin method initially developed by Kay et al. [24] has been chosen to solve this problem. Let \mathcal{T}_h be a triangulation of the domain Ω formed by finite elements K with meshsize $h = \text{diam}(K)$ such as $\mathcal{T}_h = \{K\}$ and $\bar{\Omega} = \bigcup_{K \in \mathcal{T}_h} \bar{K}$ as illustrated in Figure 2. Furthermore, we consider a subset of faces F formed by interfaces between two distinct mesh elements K_+ and K_- such as $F = \partial K_- \cap \partial K_+$ represented in red in Figure 2 and boundary faces (in blue in Figure 2) given by $F = \partial K \cap \partial \Omega$. For internal face, the unit normal \mathbf{n} is outward of K_- and inward of K_+ as it is shown in Figure 2. If \mathcal{F}_h^i gathers all interfaces and \mathcal{F}_h^b all boundary faces, the set of faces is $\mathcal{F}_h = \mathcal{F}_h^i \cup \mathcal{F}_h^b$. Finally, the local length scale at the face F noted h_F is defined according to Di Pietro and Ern [11, chap. 4 page 125].

In the formulation below, some usual notations in the context of the discontinuous Galerkin method have to be precised. First, the broken gradient ∇_h is defined by [11]

$$(\nabla_h \varphi_h)|_K = \nabla(\varphi_h|_K), \quad \forall K \in \mathcal{T}_h. \quad (35)$$

Moreover, at each interior face F , let define $\varphi_h^- = \varphi_h|_{K_-}$ the inner value and $\varphi_h^+ = \varphi_h|_{K_+}$

the outer value. We define the jump and the average of φ_h by

$$[[\varphi_h]] = \varphi_h^- - \varphi_h^+, \quad (36)$$

$$\{\{\varphi_h\}\} = \frac{\varphi_h^- + \varphi_h^+}{2}. \quad (37)$$

The discontinuous finite element space is defined by

$$X_h = \{v_h \in L^2(\Omega); v_h|_K \in P_k, \forall K \in \mathcal{T}_h\}, \quad (38)$$

with k the polynomial degree. This space belongs to the broken Sobolev space

$$H^1(\mathcal{T}_h) = \{v \in L^2(\Omega); v|_K \in H^1(K), \forall K \in \mathcal{T}_h\}. \quad (39)$$

The variational formulation of the Cahn-Hilliard problem takes the following form

Problem 2. Find $\varphi_h, \mu_h \in X_h$ such that

$$\text{Pe}^{-1} a_h(w_h, \mu_h) + b_h(w_h, \varphi_h) = 0, \text{ for } w_h \in X_h, \quad (40)$$

$$-(q_h, \mu_h) + (q_h, \varphi_h^3 - \varphi_h) + \text{Cn}^2 a_h(q_h, \varphi_h) = l_h(q_h, \varphi_h), \text{ for } q_h \in X_h, \quad (41)$$

in which

$$a_h(w_h, \mu_h) = \int_{\Omega} \nabla_h w_h \cdot \nabla_h \mu_h dV - \sum_{F \in \mathcal{F}_h^i} \int_F \{ \{ \nabla \mu_h \cdot \mathbf{n}_F \} \} [[w_h]] + \{ \{ \nabla w_h \cdot \mathbf{n}_F \} \} [[\mu_h]] - c_F [[\mu_h]] [[w_h]] dS, \quad (42)$$

$$b_h(w_h, \varphi_h) = \left(\frac{\partial \varphi_h}{\partial t}, w_h \right) + \int_{\Omega} \nabla_h \varphi_h \cdot \mathbf{u}_h w_h dV + \sum_{F \in \mathcal{F}_h^i} \int_F \left(\frac{1}{2} |\mathbf{u}_h \cdot \mathbf{n}_F| [[\varphi_h]] [[w_h]] - \mathbf{u}_h \cdot \mathbf{n}_F [[\varphi_h]] \{ \{ w_h \} \} \right) dS, \quad (43)$$

$$l_h(q_h, \varphi_h) = \text{Cn}^2 \sum_{F \in \mathcal{F}_h^b} \int_F f_h(\varphi_h) q_h dS, \text{ for } q_h \in X_h. \quad (44)$$

The details of the derivation of this variational formulation can be found in [24]. The penalty parameter c_F is equal to the product $\beta \varpi_F$ with $\beta = (k+1)(k+d)/d$ and ϖ_F

by [35]

$$\varpi_F = \begin{cases} \frac{\text{meas}(\partial K)}{\text{meas}(K)} & \text{for } F \in K \cap \partial\Omega, \\ \max\left(\frac{\text{meas}(\partial K_+)}{\text{meas}(K_+)}, \frac{\text{meas}(\partial K_-)}{\text{meas}(K_-)}\right) & \text{for } F \in K_- \cap K_+. \end{cases} \quad (45)$$

The convective term of the phase-field has been written according to the development of Di Pietro and Ern [11] with an upwinding flux approximation.

For the time discretization, a Backward Differential Formula (BDF) at order $p \leq 6$ is used. If Δt is the time step, the temporal derivative at the time $t = n\Delta t$ of the φ_h^n at the order p is given by

$$\frac{\partial \varphi_h^n}{\partial t} = \frac{1}{\Delta t} \sum_{l=0}^p \alpha_{pl} \varphi_h^{n-l} + \mathcal{O}(\Delta t^p), \quad (46)$$

for which coefficients α_{pl} can be found in the book of Süli and Mayers [37, chap. 12, page 349].

This time derivative obtained by the previous formula is introduced in $b_h(w_h, \varphi_h^n)$ leading to a source term obtained with a combination of φ_h^{n-l} with $1 \leq l \leq p$ following equation (46). Moreover, the non-linearities of the Cahn-Hilliard problem are solved using a Newton algorithm.

3.2. Spatial convergence rate

The previous problem has been implemented in the Rheolef C++ finite element library [31]. To test the numerical solver, the numerical test proposed by Kay et al. [24] is used for which the Cahn-Hilliard equation is solved with a velocity field given by

$$\mathbf{u} = f(r)(y, -x)^T, \quad \forall (x, y) \in [-1; 1]^2, \quad (47)$$

$$\text{with } f(r) = \frac{1 + \tanh[\beta(1 - 3r)]}{2}, \quad \text{and } r = \sqrt{x^2 + y^2}, \quad (48)$$

in a domain $\Omega = [-1; 1]^2$. The exact solution of the phase-field given by

$$\varphi_e = t \cos(\pi x) \cos(\pi y), \quad \forall (x, y) \in [-1; 1]^2 \text{ and } t \in]0; 1], \quad (49)$$

is imposed by adding an adequate source term in eq. (30). The range of time is taken in $[0; 0.1]$. The domain has been discretized with a regular triangular elements with 16,

23, 32, 45 and 64 elements over each Cartesian coordinate.

We perform the numerical experiment with Cahn number equal to 10^{-1} and for a Péclet number equal to 50. The temporal numerical scheme at the second order (BDF-2) has been used with a time step equal to 10^{-2} . Three polynomial degrees have been tested with $k = 1, 2$ and 3 . Errors between the numerical solution and the exact solution have been computed with L^2 norm defined as follows

$$\|v\|_{L^2,h}^2 = \int_{\Omega} v^2 dV, \quad (50)$$

Figure 3 depicts errors averaged over the time range $[0; 0.1]$ as a function of the mesh size both for the phase field and the chemical potential. For each polynomial degree, errors behave as $\mathcal{O}(h^n)$. The exponent n has been determined by non-linear fitting. For $k = 1$, n is equal to 2.08 and 2.00, for $k = 2$, $n = 3.01$ and 3.17 and for $k = 3$, $n = 4.78$ and 5.18 respectively for φ and μ . As expected, errors computed in L^2 norm behave approximately as $\mathcal{O}(h^{k+1})$ both for the phase field φ and for the chemical potential μ showing that the numerical implementation is optimal-order in error bounds as it is proved by Kay et al. [24].

4. Numerical resolution of Cahn-Hilliard and Stokes equations

The Reynolds number is assumed much less than one to neglect the inertia of the fluid. In this limit, the Navier-Stokes equations are reduced to the Stokes equations. The continuous problem is similar to the set of equations (19-21) given in § 2 in which the inertia term in the momentum equation is removed. Initial and boundary conditions for φ and μ can be written in general form as in equations (32-34). In order to take into account the boundary conditions for which velocity or stress are imposed, the frontier of Ω is shared between $\partial\Omega_D$ for which

$$\mathbf{u} = \mathbf{u}_D, \quad (51)$$

and $\partial\Omega_N$ where

$$\boldsymbol{\sigma} \cdot \mathbf{n} = \mathbf{t}_N, \quad (52)$$

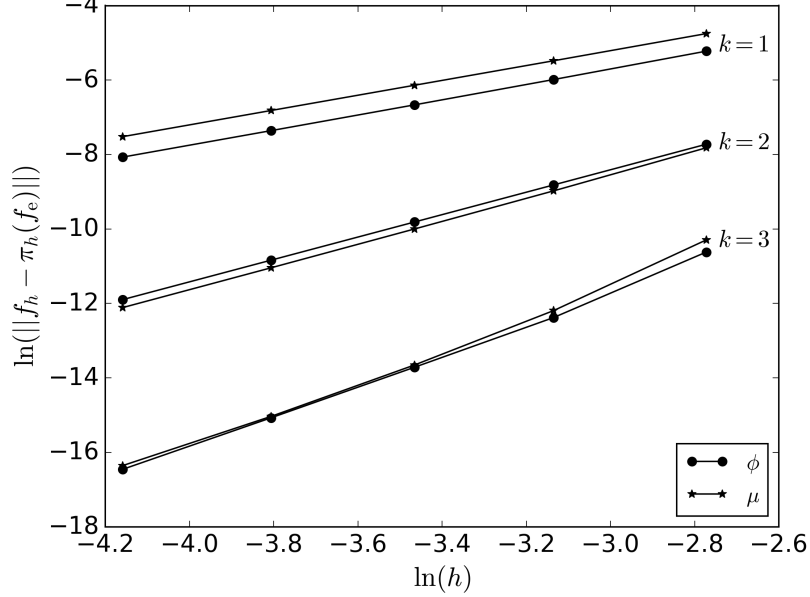


Figure 3: Errors $\|\varphi_h - \pi_h(\varphi_e)\|_{L^2, h}$ as a function of mesh size for the three polynomial degrees.

such as $\partial\Omega_D \cap \partial\Omega_N = \emptyset$ and $\partial\Omega = \partial\Omega_D \cup \partial\Omega_N$. The stress tensor is given by $-P\mathbf{I} + 2\eta(\varphi)\mathbf{D}(\mathbf{u})$ with \mathbf{I} the unit tensor. Boundary faces, \mathcal{F}_h^b , are now shared in two sub-sets $\mathcal{F}_h^{b,D}$ and $\mathcal{F}_h^{b,N}$ corresponding to $\partial\Omega_D$ and $\partial\Omega_N$ respectively.

A discontinuous Galerkin finite element method is also used to solve the Stokes equations. As it will be detailed below velocity and pressure are approximated at the same polynomial degree m . So, the discontinuous finite element spaces are defined by

$$\mathbf{V}_h = \{\mathbf{u}_h \in L^2(\Omega)^d; \mathbf{u}|_K \in P_m, \forall K \in \mathcal{T}_h\}, \quad (53)$$

$$Q_h = \{q_h \in L^2(\Omega); q|_K \in P_m, \forall K \in \mathcal{T}_h\}. \quad (54)$$

To solve the problem as a function of time, a BDF- p scheme is used to solve the phase-field equation in which the velocity field is extrapolated at the same order that the BDF scheme using the forward difference formula [1]

$$\mathbf{u}_h^{*,n} = \sum_{l=1}^p \binom{p}{l} (-1)^{l-1} \mathbf{u}_h^{n-l} + \mathcal{O}(\Delta t^p). \quad (55)$$

At the time step n , φ_h^n and μ_h^n are determined by solving the problem 2 in which the convective equation is solved using $\mathbf{u}_h^{*,n}$. Once the phase-field problem is solved, the Stokes equations have to be solved taking into account the capillary source term given by the last term of the right-hand side of (13).

4.1. Discontinuous Galerkin finite element formulation of Stokes problem

Since the Stokes equations are in quasi-steady state, the reference of the time is removed in the following to simplify the notation. The variational formulation follows the method initially introduced by Cockburn et al. [8] which has been studied theoretically by Di Pietro and Ern [11]. The heterogeneity of the viscosity needs to generalize the formulation according to the previous developments achieved in heterogeneous diffusion [11, chap. 4]. The discrete variational formulation writes:

Problem 3 (Stokes problem). Find $\mathbf{u}_h \in \mathbf{V}_h$ and $P_h \in Q_h$ such that

$$\alpha(\mathbf{u}_h, \mathbf{v}_h) + \beta(\mathbf{v}_h, P_h) = \lambda(\mathbf{v}), \quad \forall \mathbf{v}_h \in \mathbf{V}_h, \quad (56)$$

$$\beta(\mathbf{u}_h, q_h) - \gamma(p_h, q_h) = 0, \quad \forall q_h \in Q_h, \quad (57)$$

with

$$\begin{aligned} \alpha(\mathbf{u}_h, \mathbf{v}_h) = & \int_{\Omega} 2\eta \mathbf{D}_h(\mathbf{u}_h) : \mathbf{D}_h(\mathbf{v}_h) dV + \sum_{F \in \mathcal{F}_h^i \cup \mathcal{F}_h^{b,D}} \int_F [c_F \eta_F [\mathbf{u}] \cdot [\mathbf{v}] - \\ & \{ \{ 2\eta \mathbf{D}_h(\mathbf{u}_h) \cdot \mathbf{n}_F \} \}_{\omega} [\mathbf{v}_h] - \{ \{ 2\eta \mathbf{D}_h(\mathbf{v}_h) \cdot \mathbf{n}_F \} \}_{\omega} [\mathbf{u}_h] \}] dS, \end{aligned} \quad (58)$$

$$\beta(\mathbf{u}_h, q_h) = - \int_{\Omega} q_h \nabla_h \cdot \mathbf{u}_h dV + \sum_{F \in \mathcal{F}_h^i} \int_F \llbracket \mathbf{u} \rrbracket \cdot \mathbf{n}_F \{q_h\} dS, \quad (59)$$

$$\begin{aligned} \lambda(\mathbf{v}) = & \int_{\Omega} \left[\frac{\text{Bo}}{\text{Ca}} \rho_h \mathbf{g} + \frac{3}{2\sqrt{2} \text{Ca} \text{Cn}} \mu_h \nabla_h \varphi_h \right] \cdot \mathbf{v}_h dV + \\ & \sum_{F \in \mathcal{F}_h^{b,D}} \int_F \mathbf{u}_{h,D} \cdot [c_F \mathbf{v}_h - 2\eta \mathbf{D}_h(\mathbf{v}_h) \cdot \mathbf{n}] dS + \\ & \sum_{F \in \mathcal{F}_h^{b,N}} \int_F \mathbf{t}_{h,N} \cdot \mathbf{v}_h dS, \end{aligned} \quad (60)$$

$$\gamma(p_h, q_h) = \sum_{F \in \mathcal{F}_h^i} \int_F h_F \llbracket p_h \rrbracket \llbracket q_h \rrbracket dS. \quad (61)$$

The viscosity at the face F and the weighted average $\{\cdot\}_\omega$ are defined by [11]

$$\eta_F = \frac{2\eta_h^+ \eta_h^-}{\eta_h^+ + \eta_h^-}, \quad (62)$$

$$\{v_h\}_\omega = \frac{\eta_h^+ v_h^- + \eta_h^- v_h^+}{\eta_h^+ + \eta_h^-}. \quad (63)$$

Clearly, when the viscosity is constant, the usual arithmetic average is found.

4.2. Spatial and time rates of convergence

To control spatial and time rates of convergence of our numerical algorithm, we enforce a body source term in momentum and Cahn-Hilliard equations to impose an exact solution. The problem is considered in two dimensions in a space $\mathbf{x} = (x, y) \in [0; 1]^2$. According to the previous test of Dong and Shen [12], the exact phase-field solution is taken as follows

$$\varphi(\mathbf{x}, t) = \cos(\pi x) \cos(\pi y) \sin(t). \quad (64)$$

Using the definition of the chemical potential, the exact solution of μ is

$$\mu(\mathbf{x}, t) = \varphi (\varphi^2 + 2\pi^2 \text{Cn}^2 - 1), \quad (65)$$

with φ given by (64).

The two components of the velocity are chosen as following

$$u(\mathbf{x}, t) = \sin(\pi x) \cos(\pi y) \sin(t), \quad (66)$$

$$v(\mathbf{x}, t) = -\cos(\pi x) \sin(\pi y) \sin(t). \quad (67)$$

Contrary to Dong and Shen [12], the pressure has not to be set since p is imposed by the mass conservation. The two source terms which must be added in momentum equation (20) and in Cahn-Hilliard equation (20) are given in Appendix A. Remark that the velocity field is such that the rate-of-strain tensor is a diagonal tensor. The velocity solution is also used as boundary conditions while homogeneous Neumann conditions are imposed both for φ and μ .

We made tests without gravity force which is replaced by the source test enforcing the solution. The Cahn number is taken equal to 10^{-1} , the capillary number is set equal to 1 and the Péclet number at 10. The viscosity ratio is $\hat{\eta} = 10^{-1}$. To control the spatial convergence, five grids have been used with a regular triangle mesh with sizes h equal to $[1/16, 1/23, 1/32, 1/45, 1/64]$ which are uniformly logarithmically spaced. The convergence rate is determined by computing the L^2 norms both for φ , μ and \mathbf{u} . The numerical computations are achieved in time range between 0 and $\pi/2$ with a time step equal to $\pi \cdot 10^{-4}$ and with BDF-2 for the time integration scheme. Figure 4a depicts the logarithm of errors both for φ , μ and \mathbf{u} as a function of the logarithm of h . Polynomial degrees have been set equal to 1 and 2 for both φ , μ and \mathbf{u} . Whatever the polynomial degree and the field, the error behave as h^n . A non-linear fitting gives $n = 1.94, 1.91$ and 1.98 when $k = 1$ and $3.93, 3.18$ and 3.01 when $k = 2$ for φ , μ and \mathbf{u} respectively. These results prove that errors behaves approximately as $\mathcal{O}(h^{k+1})$. The error bounds of our numerical solver is consequently optimal-order in space.

The time rate of convergence is determined on a mesh grid $h = 1/32$. The Cahn, capillary and Péclet numbers are taken at the same values that previously used for the spatial rate of convergence. The time step ranges from $\pi/400$ to $\pi/100$. The final time is set equal at $\pi/2$. Only, the BDF-2 scheme has been tested. A second order polynomial approximation is taken both for φ , μ and \mathbf{u} . Figure 4b presents the logarithm of errors both for φ , μ and \mathbf{u} as a function of the logarithm of Δt . Temporal errors behave as Δt^n .

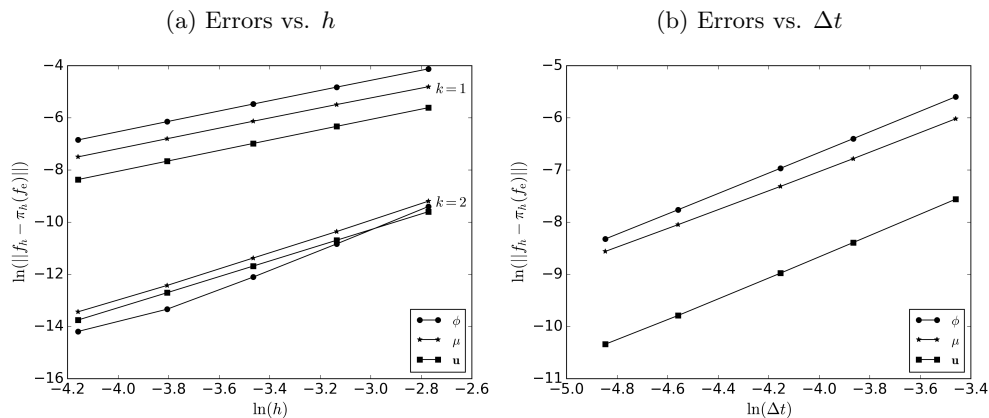


Figure 4: Rates of convergence of φ , μ and \mathbf{u} as a function of h (a) and Δt (b).

A non-linear fitting gives $n = 1.98$, 1.86 and 2.04 for φ , μ and \mathbf{u} respectively meaning that the second order is verified.

5. Numerical results on two-phase flows

In this section, two numerical examples are presented. The first case considers the drop retraction in a liquid at rest and the second will be carried out on the capillary rising to see the interaction with wall.

5.1. Ellipsoidal droplet retraction

A non-spherical droplet composed by a fluid with a dynamic viscosity μ_1 carried in another fluid at rest with a dynamic viscosity μ_2 backs to the spherical shape due to the surface tension. This phenomena is fundamental to find the constitutive equation of emulsion [27]. If the droplet is lightly deformed and in the limit of vanishing Reynolds number, the characteristic sizes of the droplet behave exponentially with time [14].

In this problem, the gravity is removed meaning that the Bond number is an irrelevant dimensionless number for this particular case. The velocity scale is chosen in order to set the capillary number equal to one. Consequently, the velocity scale is obviously equal to σ/η_1 . Only the viscosity ratio $\hat{\eta}$ remains as dimensionless number from the point of view of the physics. Beside, the Cahn and the Péclet numbers related to the phase-field modelling have to be specified. The physical length scale of interface is around few

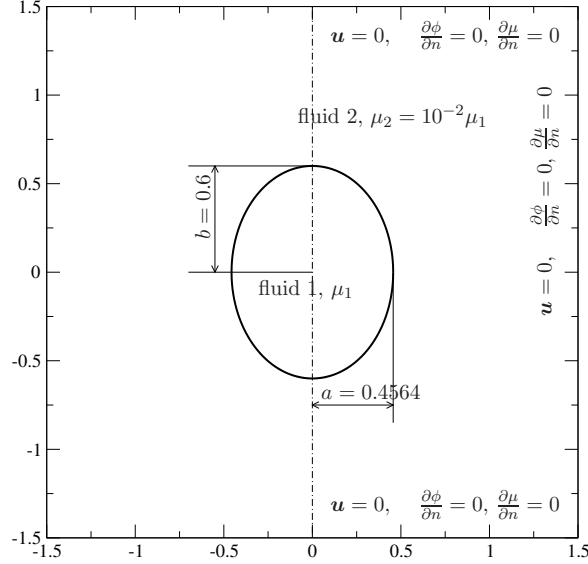


Figure 5: Initial configuration of an ellipsoidal droplet with a major axis equal to 0.6 and a minor axis equal to 0.4564. Boundary conditions both for φ , μ and \mathbf{u} are also indicated.

nanometers meaning that the ratio of this interface thickness and the droplet size is too small. Fortunately, the “sharp-interface” behavior is obtained for a larger Cahn number [43]. Here, the Cahn number is set equal to 10^{-2} . The Péclet number is taken equal to 10^2 .

Initially, the droplet shape is considered as an ellipse with a minor axis a and a major axis b . The time scale is given by $2a_\infty\eta_1/\sigma$ in which a_∞ is the radius of the sphere obtained in steady-state situation observed when the time goes to infinity. The problem is formulated in 2d-axisymmetric space. Obviously, the mass conservation leads to $a_\infty = \sqrt[3]{a^2b}$ when the axis of revolution is over the major axis. Figure 5 presents the initial configuration of the droplet. The major and minor axis have been set equal to 0.6 and 0.4564 respectively in order to have $a_\infty = 1/2$ when the time goes to infinity. The deformation of the droplet remains moderate to compare with the asymptotic solution obtained from Frankel and Acrivos [14]. At the boundaries, the no-slip condition is used for the velocity field and homogeneous Neumann condition is imposed both on φ and μ .

When the deformation is weak, the square difference between the major and the minor

axis are given according to [14, 26] by the following solution

$$\frac{(b^2 - a^2)(t)}{(b^2 - a^2)(0)} = \exp[-f(\hat{\eta})t], \quad (68)$$

with

$$f(\hat{\eta}) = \frac{80(1 + \hat{\eta})}{(2 + 3\hat{\eta})(19 + 16\hat{\eta})}, \quad (69)$$

with t without dimension.

Two numerical simulations have been made with a viscosity ratio equal to 10^{-2} . The first simulation is performed on a fix mesh grid with a mesh size equal to $1.4 \cdot 10^{-2}$. The second computation has been executed with an adaptation step with a criterion based on the order parameter φ . Figure 6 shows the behavior of $(b^2 - a^2)(t)/(b^2 - a^2)(0)$ as a function of time for $\hat{\eta} = 10^{-2}$ both for the numerical simulations performed without and with mesh adaptation. These solutions are compared with the approximate solution given by equation (68) showing that the numerical computations are in perfect agreement with the asymptotic solution.

To control the mass conservation, the relative difference between the droplet volume at each time and the initial droplet volume is plotted in Figure 7 as a function of time. Without mesh adaptation, the volume of the droplet does not change meaning that the mass conservation is perfectly observed. Contrary, the numerical computation performed with mesh adaptation presents a light change of droplet volume which remains small since at the end of the numerical run, the change is smaller than 0.09 %. The loss of mass is mainly due to the interpolation between two steps of mesh adaptation.

At the end of numerical runs, the droplet should be spherical with a radius equal to $1/2$. To control this limit, the pressure is plotted over r - and z -axis directions in Figure 8. The Laplace's law is very well verified since the pressure jump is equal to 4 as expected since the capillary number is equal to 1 and the radius is equal to $1/2$. The two curves plotted over the two orthogonal direction show that the good isotropy of the solution.

Numerical runs have been also made for other viscosity ratios. Figure 9 presents the time behavior of $(b^2 - a^2)(t)/(b^2 - a^2)(0)$ as a function of time obtained numerically for four viscosity ratios $\hat{\eta}$. The exponential decrease is very well captured numerically for all viscosity ratios. Moreover, the comparison with equation (68) shows that the role

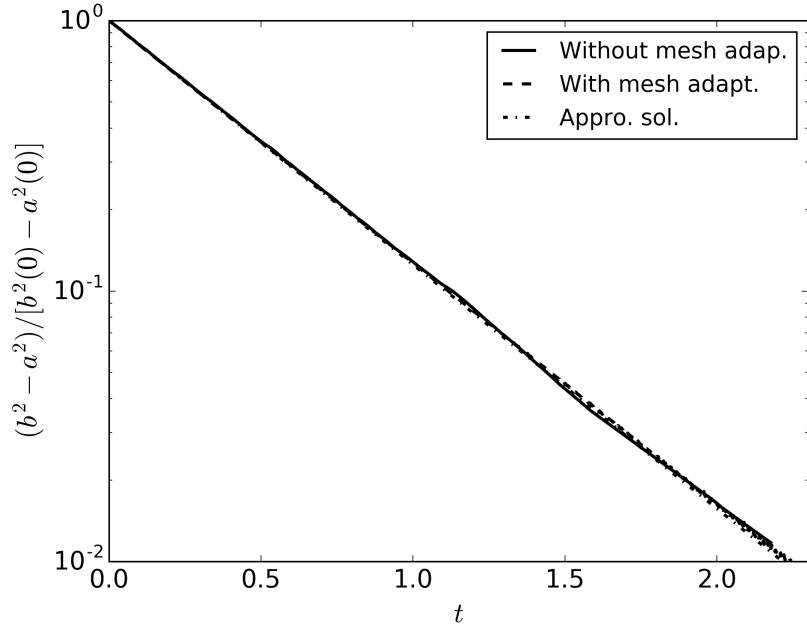


Figure 6: $(b^2 - a^2)(t)/(b^2 - a^2)(0)$ vs. t for $\hat{\eta} = 10^{-2}$ obtained numerically without mesh adaptation (solid line) and with mesh adaptation (dashed line). Dotted line curve is the approximative solution given by eq. (68).

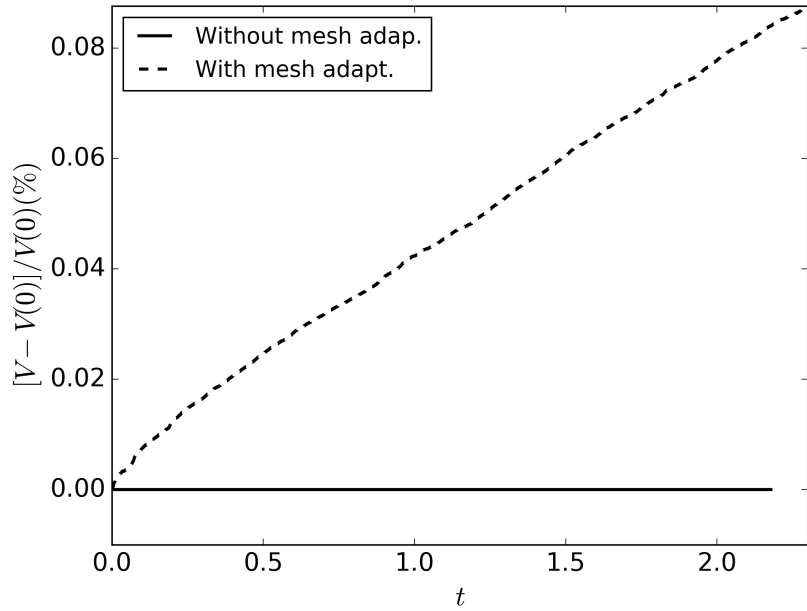


Figure 7: $[V - V(0)]/V(0)$ (%) vs. t for $\hat{\eta} = 10^{-2}$ obtained numerically without mesh adaptation (solid line) and with mesh adaptation (dashed line).

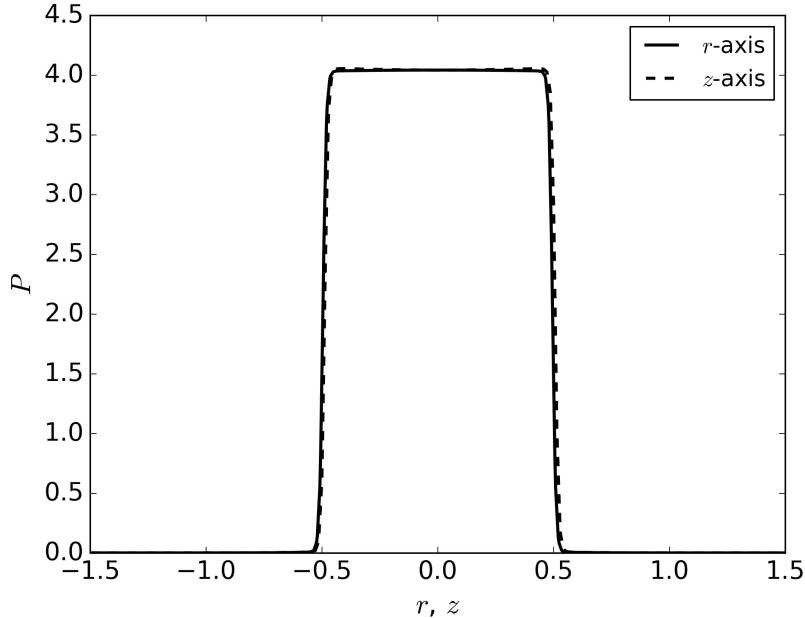


Figure 8: p vs. r or z for $\hat{\eta} = 10^{-2}$ at the end of the numerical run without mesh adaptation.

playing by the viscosity of the droplet is well established.

5.2. Capillary rising

When a liquid is introduced in a capillary tube with a diameter D , the liquid rises due to the wetting of the liquid on the tube wall. At the equilibrium, the rising height depends on the wetting angle θ , the surface tension σ , the liquid density ρ_1 , the gravity and the tube diameter. According to de Gennes et al. [10], the height over which the liquid rises can be written as follows

$$\frac{h_{\text{cap}}}{D} = \frac{4 \cos \theta}{\text{Bo}}, \quad (70)$$

in which the Bond number is defined with D as a length scale. When $\theta < \pi/2$ corresponding to “wetting” condition, h_{cap} is positif while if $\theta > \pi/2$ (“non-wetting” condition), h_{cap} is negatif meaning that the liquid goes down occurring for a liquid metal like mercury, for instance.

The dynamics of rising can be studied with the Stokes/Cahn-Hilliard equations for

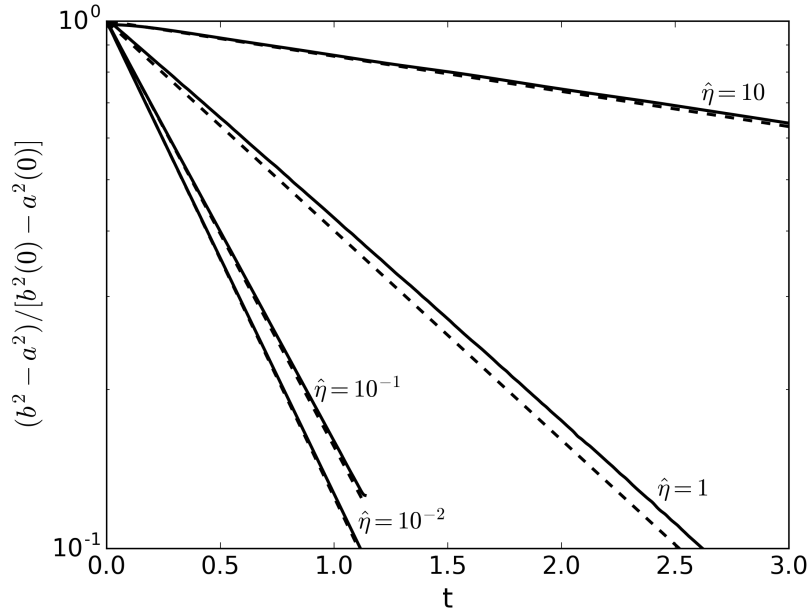


Figure 9: $(b^2 - a^2)(t)/(b^2 - a^2)(0) - a^2(0)$ vs. t for $\hat{\eta} = 10^{-2}$, 10^{-1} , 1 and 10. Solid lines are the numerical results and dashed lines come from the approximative solution given by eq. (68).

which the wetting condition can be introduced easily. We made a numerical simulation in an axisymmetric geometry depicted in Figure 10 corresponding to the one half of the tube. The problem is normalized by a length scale equal to the tube diameter. The velocity scale is taken by writing the balance between gravity and viscous forces which gives $U = \rho_1 g D^2 / \mu_1$. In this case, the capillary and Bond numbers become similar.

In the limit of vanishing Reynolds number, five dimensionless numbers have to be considered. In the previous test, the “sharp-interface” limit is very well captured when the Cahn number is an order to 10^{-2} . Consequently, the Cahn number is set equal to 10^{-2} . The Péclet number has to be taken sufficiently large to limit the diffusion. The Péclet number Pe is set equal to 50. Ratios $\hat{\rho}$ and $\hat{\eta}$ have been chosen equal to 10^{-3} and 10^{-2} respectively which are the typical values for water (fluid 1) and air (fluid 2).

The frontier of the domain depicted in Figure 10 are composed by a bottom wall localized at one radius below the initial position of the free surface. In this boundary, a pressure is imposed corresponding to the hydrostatic pressure determined with the initial position of the free surface. The vertical boundary which is at one diameter above

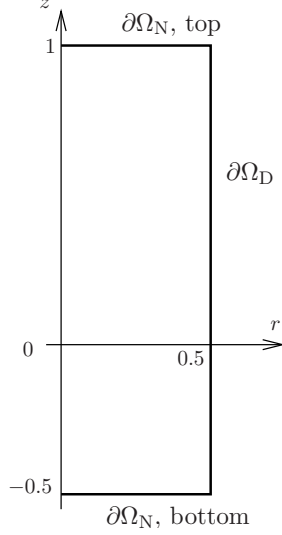


Figure 10: Geometry of a liquid rising in a tube with a radius equal to 1/2.

Boundary	φ	μ	\mathbf{u}
$\partial\Omega_N, \text{bottom}$	$\frac{\partial\varphi}{\partial n} = 0$	$\frac{\partial\mu}{\partial n} = 0$	$\boldsymbol{\sigma} \cdot \mathbf{n} = -(\hat{\rho} + \frac{1}{2})\mathbf{n}$
$\partial\Omega_N, \text{top}$	$\frac{\partial\varphi}{\partial n} = 0$	$\frac{\partial\mu}{\partial n} = 0$	$\boldsymbol{\sigma} \cdot \mathbf{n} = 0$
$\partial\Omega_D$	$\frac{\partial\varphi}{\partial n} = \frac{(1 - \varphi^2)\sqrt{2} \cos \theta}{2Cn}$	$\frac{\partial\mu}{\partial n} = 0$	$\mathbf{u} = 0$

Table 1: Boundary conditions for the numerical computation of the capillary rising of a liquid for the geometry given in Figure 10.

the initial free surface is an open boundary in which the pressure is imposed equal to zero. From the nature of these two conditions, both the bottom and top horizontal walls are designated as $\partial\Omega_N$ in Figure 10. The vertical frontier $\partial\Omega_D$ localized at $r = 1/2$ corresponds to the wall in which the non-slip condition is imposed on the velocity field. The whole conditions for both φ , μ and \mathbf{u} are summarized in Table 1.

On $\partial\Omega_D$, the wetting condition has been written according to the previous works of Jacqmin [23] and Yue et al. [43]. By this way, at the free surface corresponding to $\varphi = 0$, the wetting angle is imposed through a non-homogeneous Neumann condition on the order parameter. Initially, fluid 1 is located below the plane $z = 0$ in such of way that φ

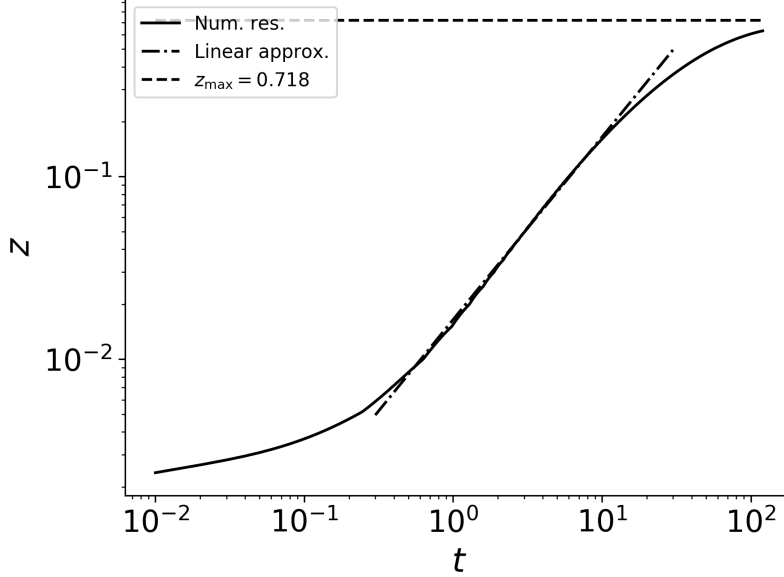


Figure 11: Contact line position as a function of time for a contact angle equal to $4\pi/9$ and $Bo = 1$.

is given by the exact solution of the Cahn-Hilliard equation in one-dimension:

$$\varphi_0(z, r) = -\tanh\left(\frac{z}{\sqrt{2} C_n}\right). \quad (71)$$

Numerical simulations have been achieved with BDF-2 temporal scheme and a time step 10^{-3} . The typical mesh size is approximately equal to 10^{-2} . Starting with a plane interface, a contact angle equal to $\theta = 4\pi/9$ (80°) is imposed for a Bond number equal to one. The position of the contact line is recorded at each time step. Figure 11 presents the position of the contact line as a function of time. The solid line is the numerical solution while the dashed-dotted line is the linear approximation. After a short time over which the static contact angle is established, the contact line rises up quasi-linearly as a function of time. When the free surface is close to the equilibrium position, the motion of the contact line becomes slower and slower. The dashed line corresponds to the position of the contact line which must be observed for $\theta = 4\pi/9$ and $Bo = 1$.

Physically speaking, when the contact angle is established on the wall, the liquid below the free surface observes a pressure which is not balanced by the weight of the liquid. Consequently, the liquid rises up until the liquid counterweights the capillary

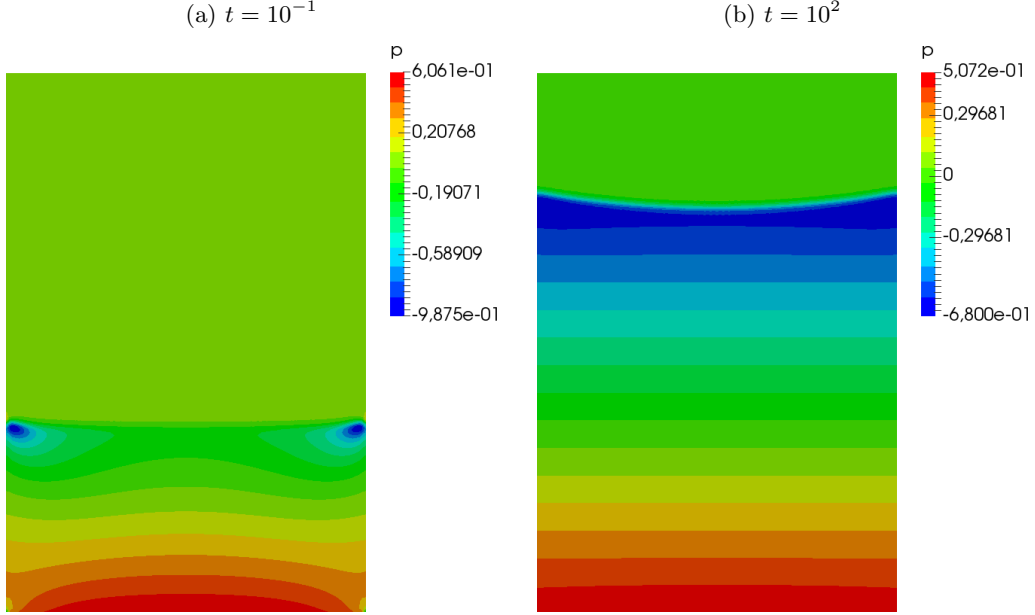


Figure 12: Pressure field in the tube at the beginning of the numerical run (a) and at the end (b) for a contact angle equal to $4\pi/9$ and $Bo = 1$.

force. In Figure 12, the pressure field is plotted at the beginning and at the end of the numerical simulation. In sub-Figure 12a recorded at the beginning of the numerical run, a low pressure is mainly observed close to the contact line. An over-pressure appears at the bottom of the tube. In sub-Figure 12b taken at the end of the numerical simulation, a hydrostatic pressure is established characterized by a curved free surface.

The position of the free surface after the rising of the liquid can be obtained easily by solving the equilibrium of the pressure due to the gravity and surface tension. If the slope of the free surface is assumed enough small, the free surface is obviously the solution of the following equation

$$\frac{1}{r} \frac{d}{dr} \left(r \frac{dz}{dr} \right) = Bo z. \quad (72)$$

The left-hand side is the curvature given by the Laplacian of the free surface. The right-hand side is the gravity forced. This last equation has been normalized for which only the Bond number is involved. The exact solution is given by

$$z = CI_0(\sqrt{Bo}r), \quad (73)$$

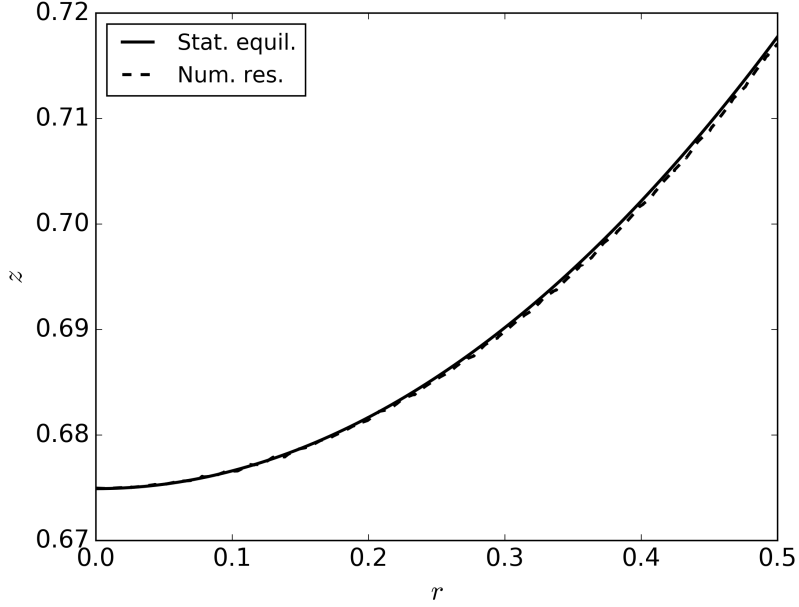


Figure 13: Geometry of the free surface, z vs. r , for a contact angle equal to $4\pi/9$ and $Bo = 1$. Solid line is the static equilibrium given by Eq. (73) and dashed-dotted line is the numerical solution.

for which, I_0 is the modified Bessel function at the zeroth order. The constant C is determined by setting the contact angle equal to θ at the wall position (in $r = 1/2$).

Figure 13 plots the z position at the function of r for the free surface obtained numerically at the end of the numerical run. The solution obtained according to the static equilibrium, Eq. (73), is also represented. The agreement between the two solutions is quite good.

The Euclidean norm of the velocity field is represented in Figure 14 at three different times (0.1, 2.5 and 100). Far away of the free surface, velocity profile is similar to a Poiseuille flow driven by the capillary rising. The amplitude of the velocity decreases with the time. When $t = 0.1$, the maximum of the Euclidean norm is approximately $4.5 \cdot 10^{-2}$ while at $t = 2.5$ $\max(\|\mathbf{u}\|)$ is equal to $1.71 \cdot 10^{-2}$ to reach $2.87 \cdot 10^{-3}$ at $t = 100$. Close to the contact line, a strong velocity gradient is observed for which the maximum of the velocity is reached close to the contact line. Nevertheless, due to the diffuse interface, the velocity remains continue.

The behavior of the axial velocity close to the contact line is shown in Figure 15

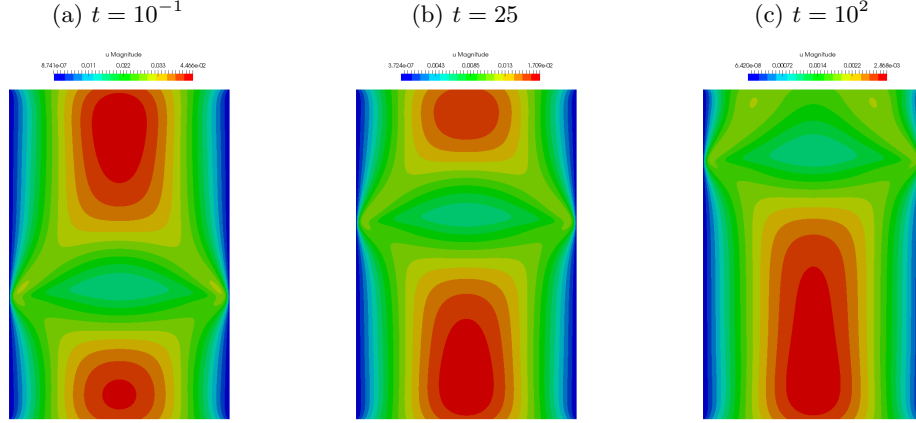


Figure 14: Velocity field in the tube at (a) $t = 10^{-1}$, (b) $t = 25$ and (c) $t = 10^2$ for a contact angle equal to $4\pi/9$ and $Bo = 1$.

where the z -component of the velocity v is plotted as a function of radial coordinate. As already pointed out, the velocity strongly increases close to the contact line mainly due to the pressure gradient driven by the capillary force. The scale over which the velocity changes is due to the diffusion length of the chemical potential coupling with the viscous dissipation. According to Jacqmin [23] and Yue et al. [43], it is expected that the length scale of diffusion is proportional to $1/\sqrt{Pe}$. In contrary, Briant and Yeomans [5] proposed another scaling of the diffusion length in $1/\sqrt[4]{Pe}$.

To control the prediction of our numerical solver, we made two supplementary runs with $Pe = 100$ and 10^3 . Velocity profiles have been extracted over the radial axis localized at the contact line at a particular time equal to 2.5. Figure 16 depicts the behavior of $v/\max(v)$ as a function of \tilde{x} defined as follows

$$\tilde{x} = \frac{(1-2r)\sqrt[4]{Pe}}{2}, \quad (74)$$

in the situation where $Bo = 1$, $Cn = 10^{-2}$. The coordinate \tilde{x} is the inner coordinate according to van Dyke [41]. Clearly, the scaling proposed by Briant and Yeomans [5] agrees very well with our numerical results. In the reference [5], the contact line dynamics is driven by a shear flow between two parallel walls while here the driven force is due to the wetting of the liquid. Consequently, our result is a confirmation of the scaling proposed by Briant and Yeomans [5].

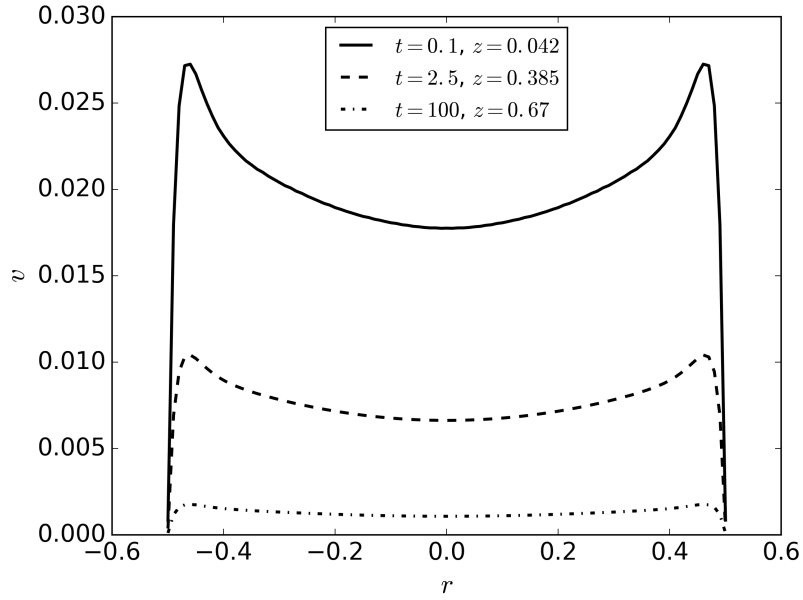


Figure 15: z -axis velocity component v vs. r , localized at the height of the contact line for a contact angle equal to $4\pi/9$ and $Bo = 1$ and for three different time.

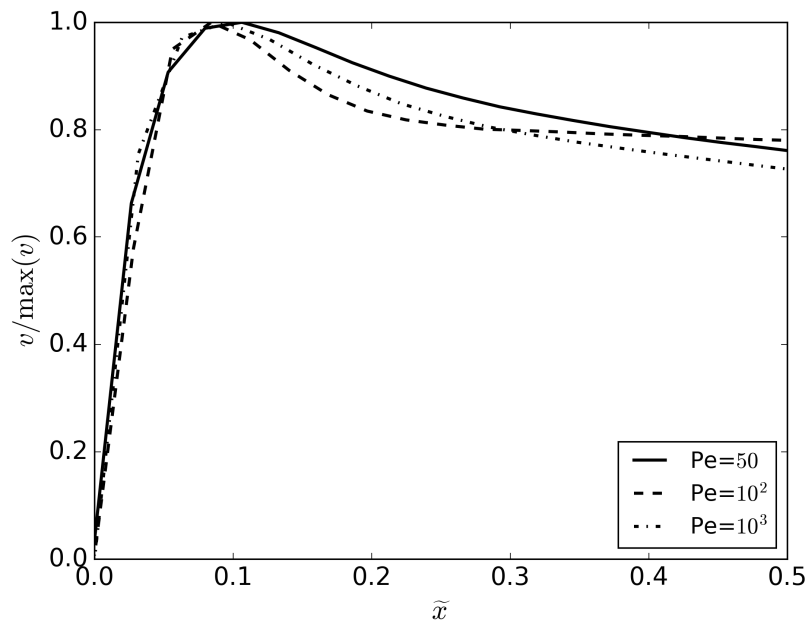


Figure 16: $v/\max(v)$ as a function of \tilde{x} at the contact line for $t = 2.5$ for $Bo = 1$ and $Pe = 50, 10^2$ and 10^3 .

6. Conclusion

This work has been devoted to a development of a numerical method to solve the coupled Stokes/Cahn-Hilliard equations in the framework of discontinuous Galerkin finite element method. First, the scheme of Cahn-Hilliard equation has been developed. The coupled equations on the order parameter and on the chemical potential are solved using a method close to the one used to solve biharmonic equations. Using an exact solution, the spatial rate of convergence has been tested which prove that the Cahn-Hilliard scheme is optimal-order in error bounds. A numerical scheme for Stokes/Cahn-Hilliard equations has been also developed for which the Stokes solver with heterogeneous viscosity has been developed. Using an exact solution, we proved that the error bounds is optimal-order both for the order parameter, the chemical potential and the velocity fields. The time rate of convergence has been also evaluated with success.

Two cases of two-phase flows have been investigated. First the droplet retraction in a liquid at rest has been numerically tested. Thanks to this test, we prove that the Stokes/Cahn-Hilliard solver conserves the mass as expected. Nevertheless, when an adaptation step is added, a small lost of mass is observed due mainly to the interpolation step between two meshes. The comparison of the droplet retraction obtained numerically and approximate solution when droplets are slightly deformed is quite good. In order to study the dynamics of the contact line physics, the problem of the capillary rising in a circular tube has been considered. The dynamics is very well reproduced and the asymptotic behavior of the static pressure equilibrium is captured. The scaling of the velocity close to the contact line has been studied.

These results show that the discontinuous Galerkin formulation is adequate to solve the coupled Stokes/Cahn-Hilliard equations with a high level of accuracy. The interaction with walls is easily taken into account and provide predictions in agreement with the physics. In near future, this numerical solver will be used to study fluid interaction with heterogeneous walls and also generalize the formulation for non-Newtonian fluids.

Appendix A. Determination of the source terms of the space rate of convergence

Appendix A.1. Source term on the Cahn-Hilliard equation

The source term on the Cahn-Hilliard equation is obviously given by

$$g(\mathbf{x}, t) = \frac{\partial \varphi}{\partial t} + \nabla \varphi \cdot \mathbf{u} - \frac{1}{\text{Pe}} \nabla \mu. \quad (\text{A.1})$$

From the exact solution of φ , eq. (64) and those of u and v , eqs. (66) and (67), the two components of the gradient of φ are given by

$$\frac{\partial \varphi}{\partial x} = -\pi u, \quad (\text{A.2})$$

$$\frac{\partial \varphi}{\partial y} = \pi v. \quad (\text{A.3})$$

From these relations, the dot product $\nabla \varphi \cdot \mathbf{u}$ is given by

$$\nabla \varphi \cdot \mathbf{u} = \pi \sin[\pi(x+y)] \sin[\pi(y-x)] \sin^2 t. \quad (\text{A.4})$$

The Laplacian of the chemical potential is easily determined from the exact solution of μ given by (65) which gives after the determination of the Laplacian of φ^3 the following relation

$$\nabla^2 \mu = -2\pi^2(2\pi^2 \text{Cn}^2 - 1)\varphi + 6\varphi\pi^2 \sin^2 t [\sin^2(\pi x) \cos^2(\pi y) + \cos^2(\pi x) \sin^2(\pi y) - \cos^2(\pi x) \cos^2(\pi y)]. \quad (\text{A.5})$$

The source term $g(\mathbf{x}, t)$ is then easily determined by addition of the partial temporal derivative of φ and the two equations (A.4) and (A.5).

Appendix A.2. Source term of the Stokes equations

The momentum equation taking into account the source term is written as follows

$$-\nabla p + \nabla \cdot [2\eta(\varphi)D(\mathbf{u})] + \frac{3}{2\sqrt{2} \text{Ca Cn}} \mu \nabla \varphi + \mathbf{f} = 0. \quad (\text{A.6})$$

As already pointed out in § 4.2, the pressure gradient has not to be taken into account to determine the forced source term \mathbf{f} . So, the source term must take into account the viscous and the capillary forces. The equation solution of u and v gives that

$$\frac{\partial u}{\partial x} = \pi\varphi, \quad (\text{A.7})$$

$$\frac{\partial v}{\partial y} = -\pi\varphi, \quad (\text{A.8})$$

$$\frac{\partial u}{\partial y} = -\frac{\partial v}{\partial x} = -\pi \sin(\pi x) \sin(\pi y) \sin t. \quad (\text{A.9})$$

From these relations, the rate-of-strain tensor is a diagonal tensor. So, the two components of \mathbf{f} are given by

$$f_x = -2 \frac{\partial}{\partial x} \left[\eta(\varphi) \frac{\partial u}{\partial x} \right] - \frac{3}{2\sqrt{2} \text{Ca Cn}} \mu \frac{\partial \varphi}{\partial x}, \quad (\text{A.10})$$

$$f_y = -2 \frac{\partial}{\partial y} \left[\eta(\varphi) \frac{\partial u}{\partial y} \right] - \frac{3}{2\sqrt{2} \text{Ca Cn}} \mu \frac{\partial \varphi}{\partial y}. \quad (\text{A.11})$$

Using the definition of the dynamic viscosity and the exact solutions of φ and \mathbf{u} , f_x and f_y take the following form

$$f_x = \pi^2 [1 + \hat{\eta} + 2(1 - \hat{\eta})\varphi] u + \frac{3\pi\mu u}{2\sqrt{2} \text{Ca Cn}}, \quad (\text{A.12})$$

$$f_y = \pi^2 [1 + \hat{\eta} + 2(1 - \hat{\eta})\varphi] v - \frac{3\pi\mu v}{2\sqrt{2} \text{Ca Cn}}, \quad (\text{A.13})$$

with φ and μ given by (64) and (65).

- [1] M. Abramowitz and I. A. Stegun. *Handbook of mathematical functions*. Dover Publications, Inc., New York, 1965.
- [2] D. M. Anderson, G. B. McFadden, and A. A. Wheeler. Diffuse-interface methods in fluid mechanics. *Annu. Rev. Fluid Mech.*, 30:139–165, 1998.
- [3] L. K. Antanovskii. A phase field model of capillarity. *Phys. Fluids*, 7(4):747–753, 1995.
- [4] V. E. Badalassi, H. D. Ceniceros, and S. Banerjee. Computation of multiphase systems with phase field models. *J. Comput. Phys.*, 190:371–397, 2003.
- [5] A. J. Briant and J. M. Yeomans. Lattice Boltzmann simulations of contact line motion. II. Binary fluids. *Phys. Rev. E*, 69:031603, 2004.
- [6] J. W. Cahn. Critical point wetting. *J. Chem. Phys.*, 66(8):3667–3672, 1977.
- [7] J. W. Cahn and J. E. Hilliard. Free Energy of a Nonuniform System. I. Interfacial Free Energy. *J. Chem. Phys.*, 28(2):258, 1958.

- [8] B. Cockburn, G. Kanschat, D. Schötzau, and C. Schwab. Local discontinuous galerkin methods for the Stokes system. *SIAM J. Numer. Anal.*, 40(1):319–342, 2002.
- [9] R. G. Cox. The dynamics of the spreading of liquids on a solid surface. Part 1. Viscous flow. *J. Fluid Mech.*, 168:169–194, 1986.
- [10] P.-G. de Gennes, F. Brochard-Wyart, and D. Quéré. *Gouttes, bulles, perles et ondes*. Belin, Paris, 2005.
- [11] D. A. Di Pietro and A. Ern. *Mathematical aspects of discontinuous Galerkin methods*. Springer-Verlag, Heidelberg, 2012.
- [12] S. Dong and J. Shen. A time-stepping scheme involving constant coefficient matrices for phase-field simulations of two-phase incompressible flows with large density ratios. *J. Comput. Phys.*, 231(17):5788–5804, 2012.
- [13] X. Feng and O. A. Karakashian. Fully discrete dynamic mesh discontinuous galerkin methods for the cahn-hilliard equation of phase transition. *Math. Comp.*, 76:1093–1117, 2007.
- [14] N. A. Frankel and A. Acrivos. The constitutive equation for a dilute emulsion. *J. Fluid Mech.*, 44(01):65–78, 1970.
- [15] M. Giaquinta and S. Hildebrandt. *Calculus of variations I*. Springer-Verlag, Berlin, 1996.
- [16] S. Gross and A. Reusken. *Numerical methods for two-phase incompressible flows*, volume 40 of *Springer series in computational mathematics*. Springer-Verlag, Berlin, 2011.
- [17] T. Gudi, N. Nataraj, and A. K. Pani. Mixed discontinuous galerkin finite element method for the biharmonic equation. *J. Sci. Comput.*, 37:139–161, 2008.
- [18] M. E. Gurtin, D. Polignone, and J. Vinals. Two-phase binary fluids and immiscible fluids described by an order parameter. *Math. Models Meth. Appl. Sci.*, 6(6):815–831, 1996.
- [19] C. W. Hirt and B. D. Nichols. Volume of fluid (VOF) method for the dynamics of free boundaries. *J. Comput. Phys.*, 39:201–226, 1981.
- [20] P. C. Hohenberg and B. I. Halperin. Theory of dynamic critical phenomena. *Rev. Mod. Phys.*, 49(3):435–479, 1977.
- [21] Chun Huh and L. E. Scriven. Hydrodynamic model of steady movement of a solid/liquid/fluid contact line. *J. Colloid Interface Sci.*, 35(1):85–101, 1971.
- [22] D. Jacqmin. Calculation of two-phase Navier-Stokes flows using phase-field modeling. *J. Comput. Phys.*, 155(1):96–127, 1999.
- [23] D. Jacqmin. Contact-line dynamics of a diffuse fluid interface. *J. Fluid Mech.*, 402:57–88, 2000.
- [24] D. Kay, V. Styles, and E. Süli. Discontinuous Galerkin finite element approximation of the Cahn-Hilliard equation with convection. *SIAM J. Numer. Anal.*, 47(4):2660–2685, 2009.
- [25] D. Legendre and M. Maglio. Comparison between numerical models for the simulation of moving contact lines. *Comput. Fluids*, 113:2–13, 2015.
- [26] P. L. Maffettone and M. Minale. Equation of change for ellipsoidal drops in viscous flow. *J. Non-Newtonian Fluid Mech.*, 78:227–241, 1998.
- [27] J. G. Oldroyd. On the formulation of rheological equations of state. *Proc. R. Soc. Lond. A*, 200(1063):523–541, 1950.

- [28] F. Pigeonneau and A. Sellier. Low-Reynolds-Number gravity-driven migration and deformation of bubbles near a free surface. *Phys. Fluids*, 23:092102, 2011.
- [29] C. Pozrikidis. *Boundary integral and singularity methods for linearized viscous flow*. Cambridge University Press, Cambridge, 1992.
- [30] T. Qian, X.-P. Wang, and P. Sheng. A variational approach to moving contact line hydrodynamics. *J. Fluid Mech.*, 564:333, 2006.
- [31] P. Saramito. *Efficient C++ finite element computing with Rheolef: vol. 2. Discontinuous Galerkin methods*. CNRS-CCSD ed., 2015.
- [32] P. Seppacher. Moving contact lines in the cahn-hilliard theory. *Int. J. Engng Sci.*, 34(9):977–992, 1996.
- [33] J. A. Sethian. *Level set methods and fast marching methods. Evolving interfaces in computational geometry, fluid mechanics, computer vision, and materials science*. Cambridge University Press, Cambridge, 1999.
- [34] J. A. Sethian and P. Smereka. Level set methods for fluid interfaces. *Annu. Rev. Fluid Mech.*, 35:341–371, 2003.
- [35] K. Shahbazi. An explicit expression for the penalty parameter of the interior penalty method. *J. Comput. Phys.*, 205(2):401–407, 2005.
- [36] Y. Sui and P. D.M. Spelt. An efficient computational model for macroscale simulations of moving contact lines. *J. Comput. Phys.*, 242:37–52, 2013.
- [37] E. Süli and D. F. Mayers. *An Introduction to Numerical Analysis*. Cambridge University Press, Cambridge (UK), 2003.
- [38] M. Ta, F. Pigeonneau, and P. Saramito. An implicit high order discontinuous galerkin level set method for two-phase flow problems. In *ICMF-2016 - 9th International Conference on Multiphase Flow*, pages 1–6, Firenze, Italy, May 22nd-27th 2016.
- [39] A. O. Unverdi and G. Tryggvason. A front-tracking method for viscous, incompressible, multi-fluid flows. *J. Comput. Phys.*, 100:25–37, 1992.
- [40] J. D. van der Waals. The thermodynamic theory of capillarity under the hypothesis of a continuous variation of density. *Verhandel. Konink. Akad. Weten.*, 1:1–56, 1893.
- [41] M. Van Dyke. *Perturbations methods in fluid mechanics*. The parabolic Press, Stanford, California, 1975.
- [42] P. Yue and J. J. Feng. Wall energy relaxation in the Cahn-Hilliard model for moving contact lines. *Phys. Fluids*, 23(1):012106, 2011.
- [43] P. Yue, C. Zhou, and J. J. Feng. Sharp-interface limit of the Cahn-Hilliard model for moving contact lines. *J. Fluid Mech.*, 645:279–294, 2010.